Nanoscale

Accepted Manuscript

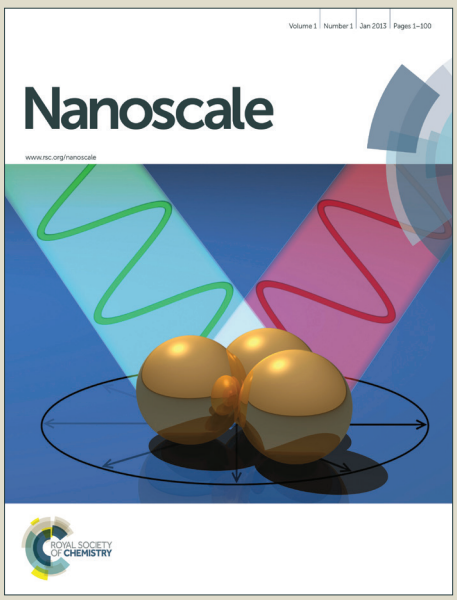

ROYAL SOCIETY OF CHEMISTRY

www.rsc.org/nanoscale

Journal Name RSCPublishing

COMMUNICATION

High Electrochemical Performance Based on TiO_2 Nanobelt@Few-Layer MoS_2 Structure for Lithium-Ion Batteries

Cite this: DOI: 10.1039/x0xx00000x

Received 00th January 2012,
Accepted 00th January 2012

DOI: 10.1039/x0xx00000x

www.rsc.org/

Minglei Mao,[a,b] Lin Mei,[a] Di Guo,[a] Lichen Wu,[a] Dan Zhang,[c] Qiuhong Li[*b] and Taihong Wang[*a]

We report a facile approach to prepare MoS_2 nanosheets coated TiO_2 nanobelts. The TiO_2@MoS_2 structure exhibits a reversible capacity of 710 mA h/g at 100 mA/g after 100 cycles with highly stable capacity retention, and bears good rate capability with a reversible capacity of 417 mA h/g at 1000 mA/g.

As a typical layered transition-metal sulfide, MoS_2 has a structure analogous to that of graphite, in which MoS_2 are held together by van der Waals forces, which can induce easy intercalation/ extraction of Li ions, lowering the energy barrier for Li ion movement.[1-3] Strongly dependent on their size and morphology, the reversible capacity of MoS_2 is greatly improved as nanoparticles or nanosheets are synthesized for lithium ion batteries.[4-8] However, their performances suffer a lot from the poor cycling stability and low rate capability. TiO_2 can be effective in improving the electrode stability, especially at high charge/discharge rates. In recent years, 1D nanostructured TiO_2 materials are regarded as promising active lithium intercalation anode materials with fast Li-intercalation/extraction because they provide shorter path lengths for both electronic and Li ionic transport, a higher electrode/electrolyte contact area, and better accommodation of the strain of Li ion intercalation/extraction.[9, 10]

Herein, we report the fabrication of few-layer MoS_2 nanosheets-coated TiO_2 nanobelts (TiO_2@MoS_2) by a simple hydrothermal method. TiO_2@MoS_2 displays excellent Li storage properties with stable charge/discharge cycling performance. In particular, TiO_2@MoS_2 shows high capacities at fast charge/discharge rates, for example, a charge capacity of 417 mA h/g at a current density of 1000 mA/g.

The synthesized TiO_2 nanobelts are of 50-150 nm wide, about 20 nm thick and several micrometers in length (Figure S1a in the Supporting Information, SI).[11, 12] After acid treatment, the surface of TiO_2 nanobelts becomes rough (Figure S1b, c). Importantly, the acid-corroded rough surface of TiO_2 nanobelts provides high energy nucleation sites for the nucleation and growth of MoS_2 nanosheets. A typical SEM image of TiO_2@MoS_2 is shown in Figure 1a. Thin MoS_2 nanosheets uniformly coat on TiO_2 nanobelts. The XRD patterns demonstrate the structure of TiO_2@MoS_2 (Figure S2). The diffraction peaks of TiO_2@MoS_2 match the standard peaks of anatase TiO_2 phase (JCPDS card no. 71-1166) and rhombohedral MoS_2 phase (JCPDS card no. 89-2905). The detected peaks can be mainly assigned to the (003), (101), (110) planes of the rhombohedral MoS_2 phase and the (101), (004), (200) and (204) planes of the anatase TiO_2 phase.

Figure 1b shows typical transmission electron microscopy (TEM) images of TiO_2@MoS_2, where the thin MoS_2 nanosheets covered TiO_2 nanobelts. The most of MoS_2 nanosheets are thin (~5 nm), less than 7 layers (Figure 1c). From the HRTEM images in Figure 1d, the lattice fringes of MoS_2 nanosheets can be clearly observed, suggesting the well-defined crystal structure. The fringes with a lattice spacing of 0.62 nm correspond to the (003) plane of MoS_2. The growth direction of the TiO_2 nanobelt is estimated to be [010]. This is supported by the HRTEM image in Figure 1e, where the lattice fringes perpendicular to the growth direction have a

spacing of 0.35 nm, which is equal to the lattice parameter in the (101) facet. In addition, the crystallographic plane of the major exposed surfaces of the nanobelts has been determined to be the (101) facet, which is the most thermodynamically stable crystal facet of anatase TiO_2.[11, 13] The energy-dispersive spectrometry (EDS) analysis of the prepared TiO_2@MoS_2 is presented in Figure 1f. It can be seen that the composite mainly contains Mo, Ti, S, and O, and the atomic ratio of Mo: Ti is about 1:2. As for Cu and C, their peaks are ascribed to the copper net and carbon film, which are used in the EDS characterization.

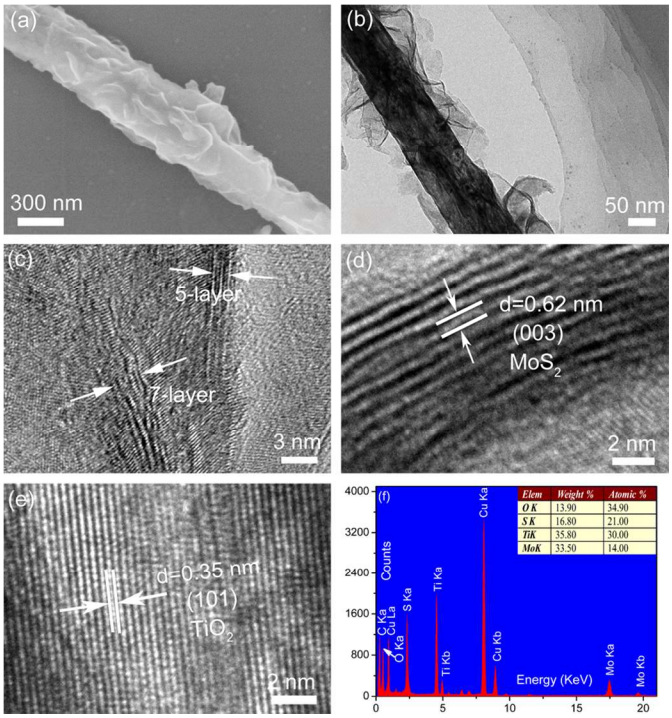

Figure 1. (a) SEM and (b) Low-magnification TEM images of TiO_2@MoS_2. (c, d) HRTEM image of MoS_2 nanosheets on the surface of TiO_2 nanobelt. (e) HRTEM image of TiO_2 nanobelt. (f) EDS of TiO_2@MoS_2.

To further investigate the surface chemical composition and valence state of the TiO_2@MoS_2, an X-ray photoelectron spectroscopy (XPS) test are performed, and the spectra are illustrated in Figure 2. The XPS spectrum shows that Mo, S, Ti，and O elements coexist in the obtained material (Figure 2a). The XPS peak for C 1s at 284.8 eV is ascribed to adventitious carbon from the XPS instrument. A typical high resolution XPS spectrum of Mo 3d is shown in Figure 2b. Two peaks at 232.0 and 228.8 eV are assigned to Mo (+4) 3d3/2 and Mo (+4) 3d5/2, respectively. The inconspicuous peak at 235.8 eV is due to Mo (+6) 3d3/2 orbit for the possibility that MoO_4^{2-} is not completely reduced during the hydrothermal procedure. Figure 2c shows the XPS spectrum of S 2p region, which can be fitted into two peaks: S 2p1/2and 2p3/2 appearing at 162.8 and 161.6 eV, respectively.[14] As for the high resolution spectrum of Ti 2p (Figure 2d), two peaks at 464.5 and 458.8 eV are attributed to Ti 2p1/2 and Ti 2p3/2, respectively. The XPS results further confirm the coexistence of MoS_2 and TiO_2 in the TiO_2@MoS_2 hierarchical structure, which agreed well with the XRD results.

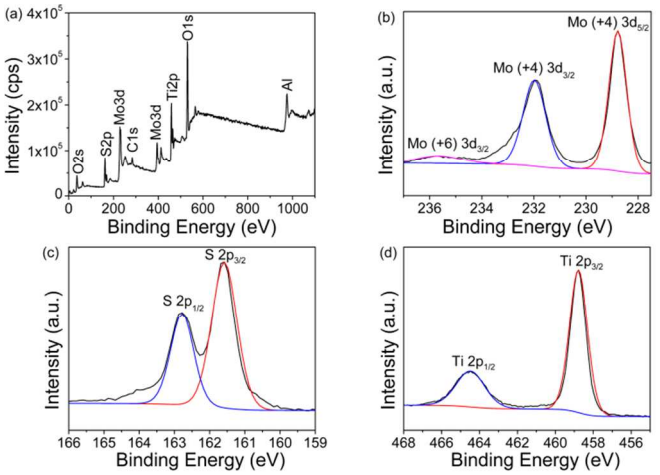

Figure 2. XPS spectra of TiO_2@MoS_2: (a) full-spectrum scan, (b) Mo 3d, (c) S 2p, (d) Ti 2p.

Electrochemical characterization was conducted to investigate the anode performances of TiO_2@MoS_2 based on two-electrode coin type cells with Li metal as the counter-electrode.[15] Figure 3a shows the cyclic voltagrams (CVs) of the TiO_2@MoS_2 electrode at a scan rate of 0.5 mV/s between 0.01 and 3 V versus Li^+/Li for the first three discharge/charge cycles. There are three cathodic peaks located at 1.61, 1.12, and 0.46 V in the first cycle of TiO_2@MoS_2 (Figure 3a). The sharp peak at 1.12 V corresponds to the phase transition from rhombohedral to octahedral phase of MoS_2 resulting from the intercalation of Li^+ ions.[16, 17] The pronounced peak located at 0.46 V corresponds to the decomposition of MoS_2 into Mo nanoparticles embedded in a Li_2S matrix, which is based on the conversion reaction:[18]

$$MoS_2+4Li^++4e^- \rightarrow Mo+2Li_2S \quad (1)$$

A major peak was observed at 1.61 V, for the Li intercalation, which is in accordance with that reported for anatase TiO_2.[19] In the anodic scan, the oxidation at 1.75 V can be attributed to the partial oxidation of Mo to MoS_2, and the following distinct peak located at 2.28 V is associated with the oxidation of Li_2S into S.[17, 20] The sharp peak at 2.1 V indicates the extraction of Li ions in anatase TiO_2. Reduction

of Ti^{4+} into Ti^{3+} during the cathodic scan and subsequent oxidation to Ti^{4+} during anodic scan indicate excellent reversibility of the anatase TiO_2 insertion host. The sharp oxidation/reduction peaks reveal the two-phase reaction mechanism during electrochemical lithium insertion/extraction according to the following reaction:[21]

$$TiO_2 + xLi^+ + xe^- \leftrightarrow Li_xTiO_2 \quad (2)$$

After the first cycle, the electrode is mainly composed of Mo and S instead of the initial MoS_2. Accordingly, in the following cycles, the reduction peak at around 2.0 V is indicative of the lithiation process of S to form Li_2S:[20, 22, 23]

$$S + 2Li^+ + 2e^- \leftrightarrow Li_2S \quad (3)$$

And the peak corresponding to the conversion reaction (1) disappears. Moreover, during the anodic sweeps in the 2nd and 3rd cycles, the peaks attributed to the Mo oxidation to MoS_2 shift positively and their intensities decrease. At the same time, the intensities of the peaks associated with the oxidation of Li_2S into S increase slightly with cycling. It suggests more Li_2S decomposes, which makes the major contribution to the reversible capacity. Nevertheless, the lithium storage kinetics of nanostructured MoS_2 is generally complex and need more investigation.[24] As for TiO_2, in the subsequent cycles, small deviations in the peak positions are noted, possibly due to structural rearrangement of TiO_2 crystal lattice.

Figure 3b displays the discharge/charge curves in the first three cycles of the TiO_2@MoS_2, measured at a current density of 100 mA/g between 0.01 and 3.0 V. For all these materials, there are three plateaus located at around 1.2, 0.6, and 1.7 V on the charge curves, suggesting the three-step lithiation process of the TiO_2@MoS_2; and the other three at around 1.7, 2.2 and 2.0 V during discharge correspond to the reversible Li^+ extraction, which is in accordance with the CV profiles. The TiO_2@MoS_2 electrode delivers an initial discharge capacity of 946 mA h/g and a subsequent charge capacity of 776 mA h/g, leading to a first cycle Columbic efficiency of 82%. The large charge capacity of TiO_2@MoS_2 electrode during the first cycle may be attributed to the formation of SEI layer and the irreversible reaction between Li and TiO_2@MoS_2 as indicated in reactions (1) and (2). During the second cycle, the TiO_2@MoS_2 hierarchical structure electrode delivers a discharge capacity of 750 mA/g and a charge capacity of 733 mA h/g with a Coulumbic efficiency of 98%.

Stable cyclic performance of electrode material is important for practical application of LIBs. The charge cycling stability of the TiO_2@MoS_2, TiO_2 nanobelts and MoS_2 nanosheets is investigated at a current density of 100 mA h/g between 0.01 and 3.0 V (Figure 3c). At a current density of 100 mA h/g, the charge capacity of the TiO_2@MoS_2 electrode remains at 710 mA h/g after 100th cycle, and Coulumbic efficiency is around 99% (Figure S3), indicating a stable cyclability. In contrast, the pure MoS_2 nanosheets can only deliver a much lower capacity of 300 mA h/g after 60 discharge/charge cycles. The charge capacity of the TiO_2@MoS_2 electrode is more than four times of the anatase TiO_2 (a reversible capacity of 174 mA h/g was retained after 100 charge-discharge cycles), and is superior to those of many recently reported MoS_2 and TiO_2 based nanostructures (Table S1 in the SI). The improved cycling performance of TiO_2@MoS_2 can be attributed to the robust composite nanostructure and the synergistic effect between the ultrathin MoS_2 nanosheets and the TiO_2. The large contact area between the building blocks and the electrolyte offers more active sites for Li^+ intercalation/extraction, resulting in high specific capacity. The TiO_2 nanobelts provide better accommodation of the strain of Li ion intercalation/extraction. Also the voids between the MoS_2 nanosheets and the TiO_2 nanobelts in the hierarchical structure accommodate the volume change, which effectively mitigates the stress and protects active materials from pulverization during the discharge/charge process. Additionally, the MoS_2 nanosheets and the TiO_2 nanobelts tended to sustain their original structure after cycling (Figure S5 in the SI), indicating that TiO_2@MoS_2 can effectively cope with the mechanical strain that was induced by iteration of the Li intercalation/extraction, resulting in stable cycle retention for the TiO_2@MoS_2 electrodes.

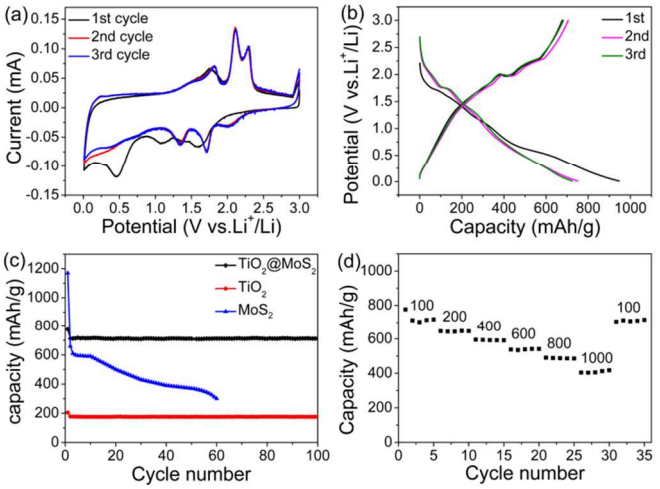

Figure 3. (a) CV curves of TiO_2@MoS_2 measured in the voltage range of 0.01-3.0 V with a scan rate of 0.1 mV/s. (b) Discharge/charge curves for the first three cycles, (c) cycling performance TiO_2@MoS_2, TiO_2 and MoS_2 tested in the range of 0.01-3.0 V vs Li^+/Li at the current density of 100 mA/g of the TiO_2@MoS_2, and (d) Rate performance at different current densities (mA/g) (charge capacity is presented).

Good rate performance is crucial to achieve high power densities in LIBs. The rate performance of the TiO_2@MoS_2 electrode is plotted in Figure 3d. It depicts fifth-cycle charge capacities of around 717, 645, 591, 541, and 485 mA h/g at current densities of 100 mA/g, 200 mA/g, 400 mA/g, 600 mA/g and 800mA/g, respectively. Even at a high current density of 1000 mA/g, the TiO_2@MoS_2 can still deliver a fifth-cycle charge capacity of 417 mA h/g, which is higher than many reported for the state-of-art anodes at 1000 mA/g (Table S1 in the SI). Moreover, the specific capacity of the TiO_2@MoS_2 electrode can recover to 710 mA h/g when the current density is returned to 0.1 A/g. The excellent rate performance of TiO_2@MoS_2 can be related to the following aspects, (1) the nanostructure avoids the aggregation while retains small dimensions and large surface area; (2) such ultrathin MoS_2 nanosheets shorten the diffusion paths of Li^+ ions, thus improving the dynamic performance of Li^+ storage.

Conclusions

In summary, we have successfully prepared few-layer MoS_2 nanosheet coated TiO_2 nanobelt by a simple hydrothermal method. The TiO_2@MoS_2 delivers promising Li storage properties with high specific capacities, stable cyclability, and good rate performances. It depicts a specific capacity of 417 mA h/g at a charge rate of 1000 mA/g, which is attractive for the development of LIBs with high power densities and high energy densities. Besides, TiO_2@MoS_2 displays a high charge capacity of 720 mAh/g at a current density of 100 mA/g, retaining almost 98% of the initial reversible capacity after 100 cycles with a high Coulumbic efficiency of 99%. These results clearly demonstrate the advantage of the TiO_2 based hierarchical structures, and further indicate a promising protocol for developing electrode materials.

Acknowledgements

This work was partly supported from the National Natural Science Foundation of China (Grant no. 61376073, 61107023), and the Specialized Research Fund for the Doctoral Program of Higher Education of China (20120161110016, 20110121120020).

Notes and references

[a] Key Laboratory for Micro-Nano Optoelectronic Devices of Ministry of Education, State Key Laboratory for Chemo/Biosensing and Chemometrics, Hunan University, Changsha 410082, P. R. China, E-mail: thwang@iphy.ac.cn
[b] Pen-Tung Sah Institute of Micro-Nano Science and Technology of Xiamen University, Xiamen, 361005, China. E-mail: liqiuhong2004@hotmail.com
[c] Department of Electronic Engineering, School of Information Science and Engineering, Xiamen University, Xiamen 361005, China

Electronic Supplementary Information (ESI) available: [details of any supplementary information available should be included here]. See DOI: 10.1039/c000000x/

1. J. N. Coleman, M. Lotya, A. O'Neill, S. D. Bergin, P. J. King, U. Khan, K. Young, A. Gaucher, S. De, R. J. Smith, I. V. Shvets, S. K. Arora, G. Stanton, H.-Y. Kim, K. Lee, G. T. Kim, G. S. Duesberg, T. Hallam, J. J. Boland, J. J. Wang, J. F. Donegan, J. C. Grunlan, G. Moriarty, A. Shmeliov, R. J. Nicholls, J. M. Perkins, E. M. Grieveson, K. Theuwissen, D. W. McComb, P. D. Nellist and V. Nicolosi, *Science*, 2011, 331, 568-571.
2. H. S. S. Ramakrishna Matte, A. Gomathi, A. K. Manna, D. J. Late, R. Datta, S. K. Pati and C. N. R. Rao, *Angewandte Chemie International Edition*, 2010, 49, 4059-4062.
3. Q. Gao, C. Giordano and M. Antonietti, *Angewandte Chemie*, 2012, 124, 11910-11914.
4. S. Ding, J. S. Chen and X. W. Lou, *Chemistry – A European Journal*, 2011, 17, 13142-13145.
5. K. Chang and W. Chen, *Journal of Materials Chemistry*, 2011, 21, 17175-17184.
6. K. Chang and W. Chen, *ACS Nano*, 2011, 5, 4720-4728.
7. H. Hwang, H. Kim and J. Cho, *Nano Letters*, 2011, 11, 4826-4830.
8. C. Zhang, Z. Wang, Z. Guo and X. W. Lou, *ACS Applied Materials & Interfaces*, 2012, 4, 3765-3768.
9. A. S. Arico, P. Bruce, B. Scrosati, J.-M. Tarascon and W. van Schalkwijk, *Nature Materials*, 2005, 4, 366-377.
10. D.-W. Kim, Y.-D. Ko, J.-G. Park and B.-K. Kim, *Angewandte Chemie*, 2007, 119, 6774-6777.
11. W. Zhou, G. Du, P. Hu, G. Li, D. Wang, H. Liu, J. Wang, R. I. Boughton, D. Liu and H. Jiang, *Journal of Materials Chemistry*, 2011, 21, 7937-7945.
12. Y. Wang, G. Du, H. Liu, D. Liu, S. Qin, N. Wang, C. Hu, X. Tao, J. Jiao, J. Wang and Z. L. Wang, *Advanced Functional Materials*, 2008, 18, 1131-1137.
13. N. Wu, J. Wang, D. N. Tafen, H. Wang, J.-G. Zheng, J. P. Lewis, X. Liu, S. S. Leonard and A. Manivannan, *Journal of the American Chemical Society*, 2010, 132, 6679-6685.
14. E. Gourmelon, O. Lignier, H. Hadouda, G. Couturier, J. C. Bernède, J. Tedd, J. Pouzet and J. Salardenne, *Solar Energy Materials and Solar Cells*, 1997, 46, 115-121.
15. S. Saadat, J. Zhu, M. M. Shahjamali, S. Maleksaeedi, Y. Y. Tay, B. Y. Tay, H. H. Hng, J. Ma and Q. Yan, *Chemical Communications*, 2011, 47, 9849-9851.
16. Y. Miki, D. Nakazato, H. Ikuta, T. Uchida and M. Wakihara, *Journal of Power Sources*, 1995, 54, 508-510.
17. J. Xiao, X. Wang, X.-Q. Yang, S. Xun, G. Liu, P. K. Koech, J. Liu and J. P. Lemmon, *Advanced Functional Materials*, 2011, 21, 2840-2846.
18. X. Fang, X. Yu, S. Liao, Y. Shi, Y.-S. Hu, Z. Wang, G. D. Stucky and L. Chen, *Microporous and Mesoporous Materials*, 2012, 151, 418-423.
19. R. Hengerer, L. Kavan, P. Krtil and M. Grätzel, *Journal of The Electrochemical Society*, 2000, 147, 1467-1472.
20. X. Fang, X. Guo, Y. Mao, C. Hua, L. Shen, Y. Hu, Z. Wang, F. Wu and L. Chen, *Chemistry – An Asian Journal*, 2012, 7, 1013-1017.
21. S. Patoux and C. Masquelier, *Chemistry of Materials*, 2002, 14, 5057-5068.

22. S.-E. Cheon, K.-S. Ko, J.-H. Cho, S.-W. Kim, E.-Y. Chin and H.-T. Kim, *Journal of The Electrochemical Society*, 2003, 150, A800-A805.
23. J. Wang, J. Yang, C. Wan, K. Du, J. Xie and N. Xu, *Advanced Functional Materials*, 2003, 13, 487-492.
24. T. Stephenson, Z. Li, B. Olsen and D. Mitlin, *Energy & Environmental Science*, 2014, 7, 209.